ACS APPLIED MATERIALS & INTERFACES

www.acsami.org

Research Article

Atomically Engineered Transition Metal Dichalcogenides for Liquid Polysulfide Adsorption and Their Effective Conversion in Li-S Batteries

Kiran Mahankali, Naresh Kumar Thangavel,* Daryna Gopchenko, and Leela Mohana Reddy Arava*

Cite This: *ACS Appl. Mater. Interfaces* 2020, 12, 27112−27121

Read Online

ACCESS | Metrics & More | Article Recommendations | Supporting Information

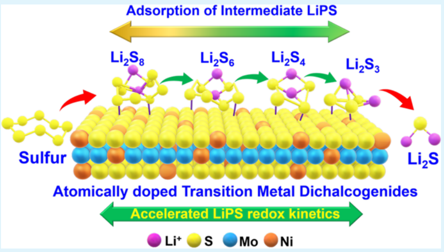

ABSTRACT: Curtailing the polysulfide shuttle by anchoring the intermediate lithium polysulfides (LiPS) within the electrode structure is essential to impede the rapid capacity fade in lithium-sulfur (Li-S) batteries. While most of the contemporary Li-S cathode surfaces are capable of entrapping certain LiPS, developing a unique electrode material that can adsorb all the intermediates of sulfur redox is imperative. Herein, we report doping of the MoS_2 atomic structure with nickel (Ni@1TMoS_2) to modulate its absorption capability toward all LiPS and function as an electrocatalyst for Li-S redox. Detailed in situ and ex situ spectroscopic analysis revealed that both Ni and Mo sites chemically anchor all the intermediate of LiPS. Electrochemical studies and detailed kinetics analysis suggested that the conversion of liquid LiPS to solid end products are facilitated on the Ni@1TMoS_2 electrocatalytic surface. Further, the employment of the Ni@1TMoS_2 electrocatalyst enhances the Li^+ diffusion coefficient, thus contributing to the realization of a high capacity of 1107 mA h g^{-1} at 0.2C with a very limited capacity fade of 0.19% per cycle for over 100 cycles. In addition, this cathode demonstrated an excellent high rate and long cycling performance for over 300 cycles at a 1C rate.

KEYWORDS: *lithium-sulfur batteries, MoS_2, Ni-doped MoS_2, polysulfide adsorption, electrocatalysis*

1. INTRODUCTION

Lithium-sulfur (Li-S) batteries turned into one of the most sought-after energy storage systems due to their appealing theoretical capacity (1673 mA h g^{-1}) and energy density (2600 W h kg^{-1}), which is ~10 times higher than any of the contemporary lithium-ion battery materials.[1−3] Conversely, the Li-S cell performance metrics including capacity, coulombic efficiency, and cycle life often deteriorated, obstructing their technology to commercialization. Manifold reasons were correlated to the cell failure; however, the diffusion of soluble sulfur intermediates into the electrolyte and their shuttling behavior between the electrodes while charging/discharging is recognized as a primary issue.[4−6] In the past two decades, various strategies have been demonstrated to mitigate the polysulfide (PS) shuttling and its associated difficulties. Though carbonaceous material-based cathodes are renowned for gaining high capacity and structural integrity, their inherent non-polar nature allows weak interaction with the polar PS, which renders shuttling effects inevitable upon extended cycles.[7−13] Anchoring of intermediate PS in the cathode surfaces is often deliberated as a key strategy as it not only controls the PS shuttling phenomenon but also improves the cycle life and round-trip efficiency.[6,14−18] Along the same line, the use of an electrocatalytic surface in the multistep sulfur redox process has shown enormous potential in the trapping of PS and accelerating the subsequent reactions, which enhances the specific capacity along with long cycle life while demonstrating excellent reversibility.[19−21]

The efficiency of electrocatalyst for Li-S redox is twofold: (i) the number of adsorption sites on the cathode and (ii) the ability of the cathode to effectively convert the LiPS. Previously, several polar functional groups including metal oxides,[12,22−25] sulfides,[26,27] and polymer matrix[28−30] have been demonstrated to chemically adsorb the intermediate PS and extend the performance of the Li-S system. On the other hand, governed by Lewis acid−base interaction, tailoring of surface acidity of metal oxides with heteroatom doping was also found to enhance the entrapment of PS.[31] However, their low surface area, inefficient electron transfer from the active sites to the underlying surface, and their poor reaction kinetics limit them from achieving stable Li-S performance.[6] Tao et al. suggested that a balance between the adsorption and diffusion of polar sulfur species should be considered as a design principle of sulfur hosts, which was revealed by a systematic comparison between various nonconductive metal oxides.[32] Nanostruc-

Received: March 9, 2020
Accepted: May 20, 2020
Published: May 20, 2020

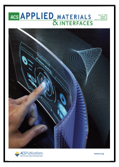

https://dx.doi.org/10.1021/acsami.0c04281
ACS Appl. Mater. Interfaces 2020, 12, 27112−27121

tured cathode surfaces with active sites either lithophilic (lithium end binding) or sulfiphilic (sulfur end binding) provide improved PS absorptivity through modulated surface binding energy during the lithiation process compared to its counterpart.[33,34] In addition, the rational design of cathodes with both lithophilic and sulfiphilic attractive polar functional groups allows the binding of PS with multiple chemical interactions and effectively convert them.[35]

However, given the fact that intermediate PS forms with different chain lengths during the reaction and undergoes manifold (electro) chemical transformations, their binding strength varies on the surface. In such circumstances, the cathode's surface can no longer have a ubiquitous anchoring effect on all the intermediate PS, and as a result some of them tend to undergo dissolution. For instance, metal sulfide[36] and metal oxide[37] cathodes demonstrated higher binding strengths specifically toward lower-order PS (Li_2S_x, $x \leq 4$) and higher-order PS like Li_2S_6 and Li_2S_8, respectively, while leaving other liquid PS susceptible to the shuttle process. Despite anchoring higher-order PS, it was also predicted that oxide cathodes may enhance undesired side reactions, leading to the dissociation of long-chain PS rather than their electrochemical conversion, where the dissociated species are responsible for the PS shuttle. Yet, in another example, TiC exhibited different binding energies toward different PS species, for instance Li_2S_8, Li_2S_7, Li_2S_5, and Li_2S demonstrated higher binding strengths, while Li_2S_4 and Li_2S_6 exhibited minimal binding.[38] To the best of our knowledge, there are no reports on cathode surfaces that tend to adsorb all the liquid intermediate LiPS and convert them to insoluble end products. Therefore, exploring the design principle for anchoring polysulfides on the cathode substrate that is capable of adsorbing all the intermediate PS while catalyzing their subsequent redox reactions is imperative to completely restrain the PS shuttle. Herein, we propose, transition metal (nickel) doping of MoS_2 nanosheets (Ni@1TMoS$_2$) to alter the adsorption strength of the cathode toward LiPS to effectively curtail the PS shuttle phenomenon, as shown in Figure 1. The adsorption capability of Ni@1TMoS$_2$ toward various intermediate LiPS was investigated using ultraviolet−visible spectroscopy and nuclear magnetic resonance. Further in situ Raman spectroscopy studies were conducted to elucidate the PS anchoring mechanism of this novel electrocatalyst. Finally, the electrochemical properties of Ni@1TMoS$_2$ nanosheets were studied in detail using cyclic voltammetry and galvanostatic charge−discharge studies. We believe that electrocatalysis of PS using inexpensive materials such as Ni@1TMoS$_2$ nanosheets will open a new avenue for developing efficient energy storage technologies.

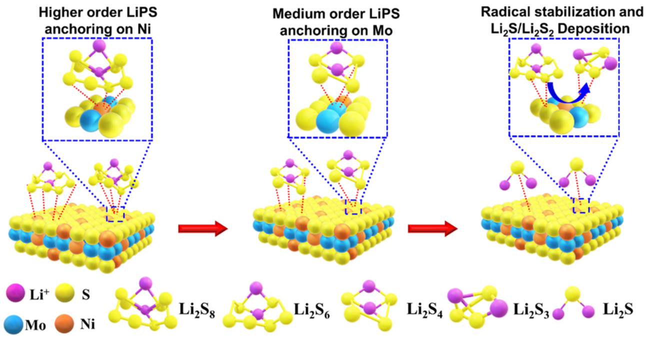

Figure 1. Schematic representation demonstrating the effective anchoring of LiPS (Li_2S_x, $x \leq 8$) on various active sites of the Ni@1TMoS$_2$ surface.

2. EXPERIMENTAL METHODS

2.1. Synthesis of Ni@1TMoS$_2$. The Ni@1TMoS$_2$ electrocatalyst was synthesized using Anderson-type POM nanoclusters ($NiMo_6$) by a sulfurization hydrothermal reaction.[39] Initially, the $(NH_4)_4[NiH_6Mo_6O_{24}]\cdot 5H_2O$ ($NiMo_6$) precursor was prepared by dissolving Mo_7 (4.2 mmol) in 80 mL of DI water with subsequent heating at 100 °C. Simultaneously, $Ni(NO_3)_2\cdot 6H_2O$ (4 mmol) was dissolved in 20 mL of DI water and was added to the above solution under stirring. The mixture was thoroughly stirred under heating until a dark green solution appeared. The obtained product was then separated by evaporation and filtration, which was recrystallized twice in hot water (80 °C) with subsequent drying under vacuum. In the next step, the $NiMo_6$ precursor (0.042 mmol) was mixed with thioacetamide (1.065 mmol) in 10 mL of H_2O. The solution was then transferred to a Teflon-lined autoclave and heated at 180 °C for 24 h. The final product obtained was subsequently washed with DI water 3 times and dried under vacuum at 80 °C. For comparison, 1TMoS$_2$ was also prepared in a similar fashion but without the incorporation of Ni.

2.2. Preparation of Electrocatalytic Cathodes. The binder-free electrode materials for the Li-S batteries were prepared by vacuum infiltering the electrocatalysts into a conductive carbon gas diffusion layer (GDL). In this route, 20 mg of the active material was uniformly dispersed in 10 mL of isopropyl alcohol and ultrasonic treatment was performed for 3 h. Then, the solution was infiltered into a GDL paper, under vacuum, which was subsequently dried under vacuum conditions at 80 °C overnight.

2.3. Preparation of Lithium Polysulfides (LiPS). For the LiPS adsorption studies, 1 mM lithium polysulfide (Li_2S_4, Li_2S_6, Li_2S_8) solutions were made by reacting stoichiometric amounts of Li_2S and sulfur in 1:1 v/v 1,3-dioxolane and 1,2-dimethoxyethane at 50 °C under constant stirring overnight. For NMR studies, 50 mM LiPS were prepared by mixing stoichiometric amounts of Li_2S and sulfur in NMR-grade dimethyl sulfoxide (DMSO) solvent. The blank electrolyte was prepared by mixing 1 M LiTFSI and 0.1 M $LiNO_3$ salts in 1:1 v/v 1,3-dioxolane and 1,2-dimethoxyethane under magnetic stirring.

2.4. Coin Cell Fabrication. Standard 2032-coin cells were assembled inside an argon-filled glovebox (oxygen and moisture levels maintained below 0.1 ppm) to study the electrochemical performance of the electrocatalysts against sulfur and intermediate LiPS redox reactions. The electrocatalyst-infiltered GDL was cut into circular disks of diameter 12.7 mm to be used as a positive electrode, and the catalyst loading was around 10% of the total cathode weight. Subsequently, the active material was introduced into the cathode through the melt-diffusion process, by adding 1.5 mg cm^{-2} of sulfur on the cathode followed by heating it to 155 °C under an Ar atmosphere. Coin cells were then assembled using this sulfur-introduced cathode and Li metal foil as an anode with Celgard as a separator wetted with an appropriate amount of the blank electrolyte. Further, coin cells were also assembled with GDL paper alone, without the addition of any electrocatalysts for control studies.

2.5. Characterizations. Transmission electron microscopy (TEM) images were recorded on a JEOL 2010 transmission electron microscope at an acceleration voltage of 200 kV using a LaB_6 filament gun. X-ray diffraction (XRD) patterns of the as-prepared samples were collected at a scan rate of 0.05 s^{-1} using Cu Kα radiation (Rigaku Miniflex II X-ray diffractometer). Adsorption studies between electrocatalysts and polysulfides were then performed on a Shimadzu UV-2600/2700 UV−visible spectrophotometer. Raman spectra were recorded by the Andor Shamrock 500i system with a 532 nm green laser (Nd:YaG source). Nuclear magnetic resonance (NMR) spectroscopic studies were carried out on an Agilent 400 MHz NMR instrument. X-ray photoelectron spectra of the as-prepared materials were collected using a PHI Quantera spectrophotometer, and open-source XPS peak fit 4.1 software was used for deconvoluting the spectra. Electrochemical impedance spectroscopy and cyclic

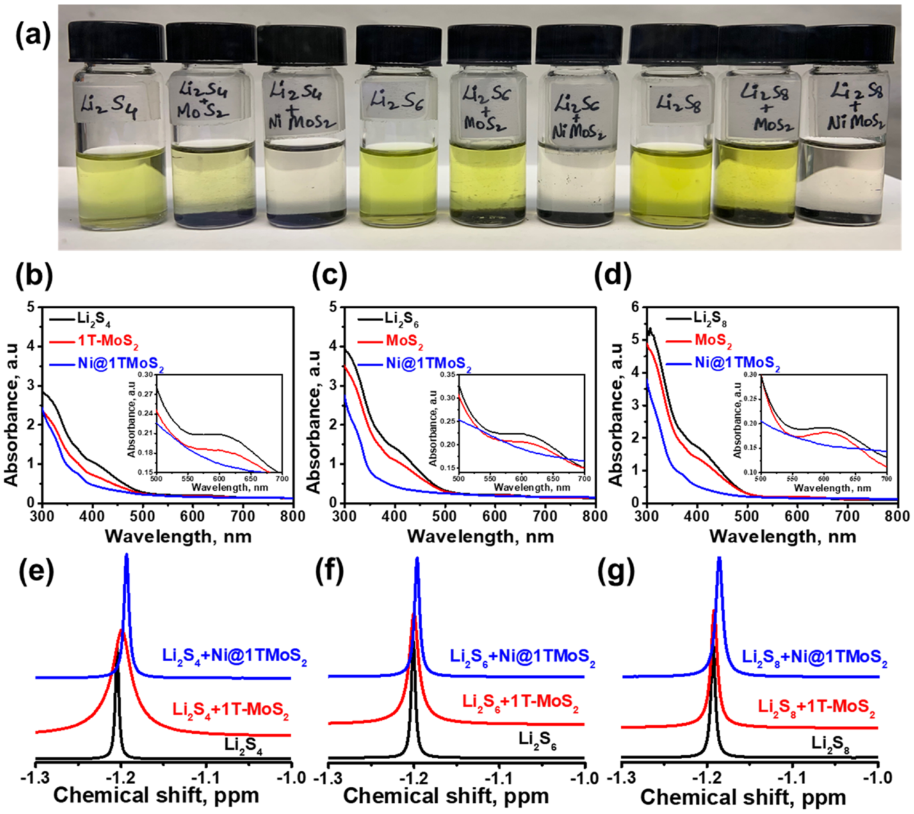

Figure 2. (a) Digital photograph of polysulfide adsorption testing for $1TMoS_2$ and Ni@$1TMoS_2$ cathodes. (b−d) UV−vis absorption spectra with insets of the zoomed area and (e−g) NMR spectra recorded with and without the addition of $1TMoS_2$ and Ni@$1TMoS_2$ in (b,e) Li_2S_4, (c,f) Li_2S_6, and (d,g) Li_2S_8 solutions.

voltammetric studies were conducted using a Biologic SP300 bipotentiostat, and galvanostatic charge−discharge was performed in the potential range of 2.8−1.7 V in an ARBIN cycle life tester.

2.6. Visual Inspection and UV−Vis Spectroscopic Studies. For this study, 1 mg of both MoS_2 and Ni@$1TMoS_2$ materials were added to 2 mL of 1 mM LiPS (Li_2S_4, Li_2S_6, and Li_2S_8 in DOL/DME solution) in an Ar-filled glovebox. The samples were rested for 3 h, and visual inspection was then performed. Subsequently, 2 mL of supernatant solution from each of the samples was collected and transferred to UV−vis cuvettes, which were thoroughly sealed inside the glovebox.

2.7. In Situ Raman Studies. In situ Raman spectroscopic studies were carried out in an in-house-built three-electrode electrochemical cell with a 532 nm green laser (Nd:YaG), as per procedures described in our previous reports.[40−42] The active material (Ni@$1TMoS_2$) was infiltered into GDL as described earlier, and after thorough drying, sulfur was melt-diffused into the electrode. The catalyst-modified GDL was later immobilized in the cell and acted as a working electrode, while lithium metal foil served as both counter and reference electrodes, and a freshly prepared blank electrolyte was used. The whole setup was made inside an argon-filled glovebox in an environmental chamber, which was later transferred to the Raman instrumentation. The galvanostatic discharge was performed in the potential region between OCV of ∼2.7 and 1.7 V vs Li/Li^+ using a Biologic SP-300 electrochemical workstation. The Raman spectrum was recorded continuously for every 5 min, with acquisition time and cycle time of 30 s each. All the obtained band intensities were previously baseline-corrected.

3. RESULTS AND DISCUSSION

The Ni@$1TMoS_2$ sample was synthesized via a simple and facile hydrothermal method. For better comparison, the $1TMoS_2$ sample was also prepared using a similar methodology without the Ni dopant. The as-synthesized Ni@$1TMoS_2$ along with its counterpart was systematically characterized using TEM, EDAX, XRD, and Raman studies, as shown in Figures S1−S3. The TEM images (Figure S1) evidence that Ni@$1TMoS_2$ samples' morphology consists of discrete and extensive wrinkles at the edges, which entails the narrow distribution of an ultrathin structure of the nanosheets. EDAX mapping of the samples (Figure S2) confirmed the successful doping of MoS_2 by Ni, and its content was found to be around 4.19%. In addition, the XRD pattern (Figure S3a) clearly depicts three characteristic diffraction peaks at $2\theta = 13.6$, 32.5, 35.1, and 57.2^0, which corresponds to the (002), (100), (102), and (110) planes of hexagonal MoS_2. Further, Raman spectra of the samples were collected to confirm the doping of Ni onto $1TMoS_2$. As shown in Figure S3b, the $1TMoS_2$ (black curve) displayed prominent characteristic Raman vibrational modes located at 146, 212, and 335 cm^{-1}. However, a slight shift in the peaks and changes in the peak intensities were observed for the Ni@$1TMoS_2$ samples in comparison with undoped $1TMoS_2$, indicating successful doping of secondary metals.[39] Further, to understand the chemical composition and to confirm the Ni doping in the MoS_2 structure, we have performed an X-ray photoelectron spectroscopy (XPS) study on the Ni@$1TMoS_2$ and compared it with the $1TMoS_2$ material (Figures S4 and S5). The XPS survey spectrum of Ni@$1TMoS_2$ shows C, O, Mo, S, and Ni peaks at the corresponding binding energies (Figure S4a). Meanwhile, $1TMoS_2$ exhibits C, O, Mo, and S peaks at the respective binding energies (Figure S4b). The presence of Ni atoms in the Ni@$1TMoS_2$ survey spectrum clearly demonstrates the possible Ni compositions in those samples. The deconvoluted

Mo 3d spectra, as shown in Figure S5a,a', consist of two characteristic peaks at 228.72 and 231.90 eV corresponding to Mo^{4+} $3d_{5/2}$ and Mo^{4+} $3d_{3/2}$, which are typically assigned to the 1T phase of MoS_2.[43,44] Similarly, the S 2p spectrum of $1TMoS_2$ was deconvoluted into two major peaks 161.80 (S $2p_{3/2}$) and 162.94 eV (S $2p_{1/2}$)[45] (Figure S5b,b'). Interestingly, the Mo 3d and S 2p spectra of the $Ni@1TMoS_2$ displayed a positive shift of ∼0.30 compared to $1TMoS_2$, depicting the enhancement in the electronic density of MoS_2 due to the successful incorporation of the Ni element. Further, the Ni 2p spectrum shows two strong peaks at 854.26 eV (Ni $2p_{3/2}$) and 871.9 eV (Ni $2p_{1/2}$), which originate from the metal−sulfide bond in $Ni@1TMoS_2$ (Figure S4c,c'). More importantly, the peak centered at 854.3 eV is a characteristic feature of the NiMoS structure, which indicates successful doping of Ni into the lattice of MoS_2 nanosheets.[46,47] Overall, the XPS characterization confirms (i) the successful synthesis of the $1TMoS_2$ phase and (ii) Ni doping into the $1TMoS_2$ structure.

3.1. LiPS Anchoring on $Ni@1TMoS_2$.

To understand the chemical adsorption capability of the $Ni@1TMoS_2$ surface for the LiPS, we carried out a systematic adsorption test by adding 1 mg of $Ni@1TMoS_2$ separately into 2 mL of 1 mM LiPS solutions (Li_2S_4, Li_2S_6, and Li_2S_8) and compared them with $1TMoS_2$ materials. After 3 h of aging, visual inspection of the samples (Figure 2a) demonstrated that the $Ni@1TMoS_2$ nanosheets showed a very strong anchoring for all the LiPS as evidenced by an obvious color fade, Figure 1. Meanwhile, the $1TMoS_2$ sample displayed strong adsorption behavior toward lower-order LiPS (Li_2S_4) compared to the higher-order LiPS, which agreed well with the previous reports.[48] In order to obtain spectral evidence on the strong anchoring ability of $Ni@1TMoS_2$ toward LiPS, we have carried out ultraviolet−visible (UV−vis) spectroscopy to monitor absorbance changes in the LiPS solutions after adding the electrocatalysts. All UV−vis spectra were collected using supernatants of LiPS solution in the range of 300−800 nm, as shown in Figure 2b−d. As observed in the UV−vis spectrum, a broad peak was observed at 420 nm corresponding to S_4^{2-} species (black line),[49] which was found to decrease with the addition of $1TMoS_2$ (red line), which further decreased in the case of $Ni@1TMoS_2$ (blue line). Similarly, it can be clearly seen that the absorbance peaks of Li_2S_6 and Li_2S_8, in the visible-light range, disappeared with the addition of $Ni@1TMoS_2$. In contrast, only a slight weakening of adsorption intensities of these PS was evidenced with the addition of $1TMoS_2$. These results are in good agreement with the visual inspection data and demonstrate an exceptional LiPS adsorption capability by the $Ni@1TMoS_2$. Also, to quantitatively investigate the LiPS adsorption capabilities of the $1TMoS_2$ and $Ni@1TMoS_2$ materials, we have calculated the amount of LiPS anchored on their surfaces using the Beer−Lambert law: $A = L\varepsilon c$, where A is the absorbance of the sample, L is the light path length, ε is the molar absorptivity, and c is the concentration.[50−52] Given that the values of L and ε are constant for a particular LiPS sample and the absorbance is directly proportional to the concentration, polysulfide adsorption capability was calculated based on the LiPS concentration remaining in the supernatant solution. From Table S1, it is evident that the $Ni@1TMoS_2$ offers a LiPS adsorption approximately 3−5 orders of magnitude higher than that of the $1TMoS_2$.

To further evidence the adsorption capablity of $Ni@1TMoS_2$, given that the NMR chemical shift is highly dependent on the surrounding environment,[53] we have performed Li^7 NMR spectroscopic studies to understand the nature of the interaction between the electrocatalysts and the LiPS species. In NMR spectroscopy, the increasing line width is generally attributed to the greater number of surrounding molecules interacting with the nuclei, while the downfield shift is a result of the weakness of nucleus electron density with neighboring atoms.[54−56] As shown in Figure 2e−g, the Li^7 NMR spectrum of all the as-prepared LiPS, Li_2S_8, Li_2S_6, and Li_2S_4, displayed a narrow line signal at approximately −1.20 ppm, indicating that all LiPS have a similar nuclei environment.[54] In the case of the $1TMoS_2$ material, a downward shift in the NMR spectra was observed only in the case of Li_2S_4 solution along with line width broadening features. Meanwhile, other LiPS, viz., Li_2S_8 and Li_2S_6 showed a very negligible peak shift without changes in shape. Though the interaction between bare $1TMoS_2$ and higher-order LiPS, like Li_2S_8 and Li_2S_6, is minimal as depicted by NMR, these species can undergo spontaneous disassociation on the surface of MoS_2.[4] Such a phenomenon can produce short-chain LiPS, which can exhibit higher binding energies toward MoS_2 and explains the reason for the decreased adsorption in the case of UV−vis and visual testing for lower-order LiPS. In sharp contrast, in the presence of $Ni@1TMoS_2$, the NMR spectrum of all LiPS showed a downward shift along with an increase in peak width. These results indicate the strong binding of all liquid intermediate LiPS on the $Ni@1TMoS_2$ surface. Previously, MoS_2 demonstrated higher adsorption activity on its edge sites, due to their unsaturated nature, compared to its basal sites. On the other hand, Ni atom doping onto the basal and edge planes of MoS_2 leads to the formation of Ni−Mo interaction. In addition, it has been predicted that the doping of MoS_2 by Ni causes a modification in the electronic structure and electron transfer process arising from the formation of several impure states, in the band gap of $Ni@1TMoS_2$, around the Fermi level and valance band.[55−57] The newly induced states indicate a p-d hybridization of p electrons in S atoms and d electrons in Ni and Mo atoms, resulting in the availability of surplus electrons on $Ni@1TMoS_2$. Such a process ultimately leads to uniformly spread charges over the basal plane of $Ni@1TMoS_2$, which has shown significant enhancement in the LiPS adsorption capability along with an increase in number of active sites.[58,59] Additionally, previous reports suggest that Ni exhibits strong binding energies of −9.10, −6.52, and − 5.39 eV toward Li_2S_8, Li_2S_6, and Li_2S_4, respectively.[60] On the other hand, MoS_2 has been[48,61] demonstrated to show higher binding energies toward lower-order PS like Li_2S_4, Li_2S_2, and Li_2S. Hence, the Ni-doped MoS_2 is expected to show a synergetic effect toward binding all PS (Li_2S_x, $x \leq 8$) and results in an enhanced chemical interaction between the electrocatalyst and Li atoms in Li_2S_x. Such an effort is expected to curb the dissolution of medium-order PS, which are known to be responsible for the polysulfide shuttle phenomenon and subsequent capacity fade.

3.2. In Situ Raman Spectroscopy.

To further corroborate the chemical bond formation between the $Ni@1TMoS_2$ and LiPS and to understand the reaction mechanism along with changes in the chemical state of sulfur, in situ Raman spectroscopic studies were carried out. Figure 3 depicts the in situ Raman spectra obtained for the sulfur/$Ni@1TMoS_2$ cathode surface during the discharge from open circuit potential of 2.72 to 1.7 V vs Li/Li^+. The Raman spectrum exhibits three characteristic Raman bands at 150, 219, and 470 cm^{-1} corresponding to S_8 (Table S2) at the initiation of discharge, which gradually decreases and finally disappears

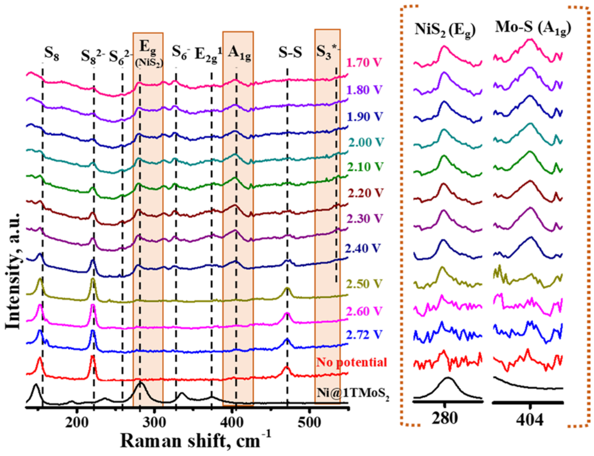

Figure 3. In situ Raman measurements during the Li-S discharge process on Ni@1TMoS$_2$ cathode surface in the potential regions of 2.7 to 1.7 V vs. Li/Li$^+$. Laser: a 532 nm green laser (Nd:YaG source).

with decreasing potential. Simultaneously, at ∼2.40 V, a new peak emerged at 278 cm^{-1}, which can be ascribed to the formation of E$_g$ vibrational mode corresponding to the in-phase stretching of NiS (a typical pyritic structure).[62,63] In addition, the emergence of another peak at ∼404 cm^{-1} corresponding to the out-of-plane Mo−S mode (A$_{1g}$) was also observed at the same potential. This result demonstrates the increase in number of adsorption sites for the intermediate LiPS, which can be due to the doping of Ni atoms into the MoS$_2$, especially on the top sites of the basal plane.[57] Further, at a discharge potential of 2.30 V, the appearance of a new Raman band at 256 cm^{-1} was observed, which can be ascribed to the formation of S_6^{2-} species. More importantly, with a further reduction in the discharge potential, S_6^{2-} dissociates into a trisulfur radical ($S_3^{\cdot-}$) as evidenced by the emergence of a Raman band at 534 cm^{-1}.[64] This highly reactive $S_3^{\cdot-}$ radical was reported to be an active participant in the PS shuttle phenomenon causing parasitic reactions with the Li anode during cycling.[49,65] Interestingly, as depicted by UV−vis spectroscopy (Figure 2b−d inset), the absorbance intensity of the $S_3^{\cdot-}$ radical (at 620 nm[49,66,67]) is negligible in the case of Ni@1TMoS$_2$, implying that it has a high affinity and strong adsorption ability toward the radical species. Hence, the $S_3^{\cdot-}$ radicals formed during the Li-S discharge process can be spontaneously entrapped by the Ni@1TMoS$_2$ electrocatalyst, which effectively stabilizes them through interaction. Such stabilization of radical species onto metal oxide surfaces was previously evidenced in the case of superoxides[68] but was never reported in the case of LiPS. Subsequently, further reduction of LiPS into final discharge products can thus proceed on the catalyst surface, thereby effectively curbing the PS shuttle. Thus, the Raman results demonstrate that sulfur species evolving during the Li-S discharge process undergo facile binding both on Ni and Mo, while the highly shuttle-active radical species are also anchored by Ni@1TMoS$_2$, which can result in enhanced cycle life.

3.3. Evaluation of Electrocatalytic Effect of Ni@1TMoS$_2$ on LiPS Redox Reactions.

To understand the catalytic effect of Ni@1TMoS$_2$ on intermediate LiPS reaction kinetics, symmetric cells made with 0.2 M Li$_2$S$_6$ catholytes were assembled with identical working and counter electrodes. Symmetric cells with 1TMoS$_2$ and GDL electrodes were also fabricated and studied for control experiments. Figure 4a shows the recorded electrochemical impedance spectra (EIS) of the symmetric cells. The resultant Nyquist plots display a semicircle in the high-frequency region, which serves as direct evidence for the charge transfer process and assists in quantifying the reaction kinetics. The Ni@1TMoS$_2$ cells exhibited the lowest charge transfer resistance (6.1 Ω), while the 1TMoS$_2$ and GDL electrodes showed 10.8 and 12.5 Ω, respectively. Next, cyclic voltammetry was performed in the potential region of +1 to −1 V at a scan rate of 5 mV s^{-1} on the symmetric cells assembled with (Figure 4b) and without (Figure 4c) Li$_2$S$_6$ catholytes. The symmetric cells without Li$_2$S$_6$ delivered negligible capacitive current rather than any faradic redox peak currents. On the other hand, the voltammogram of

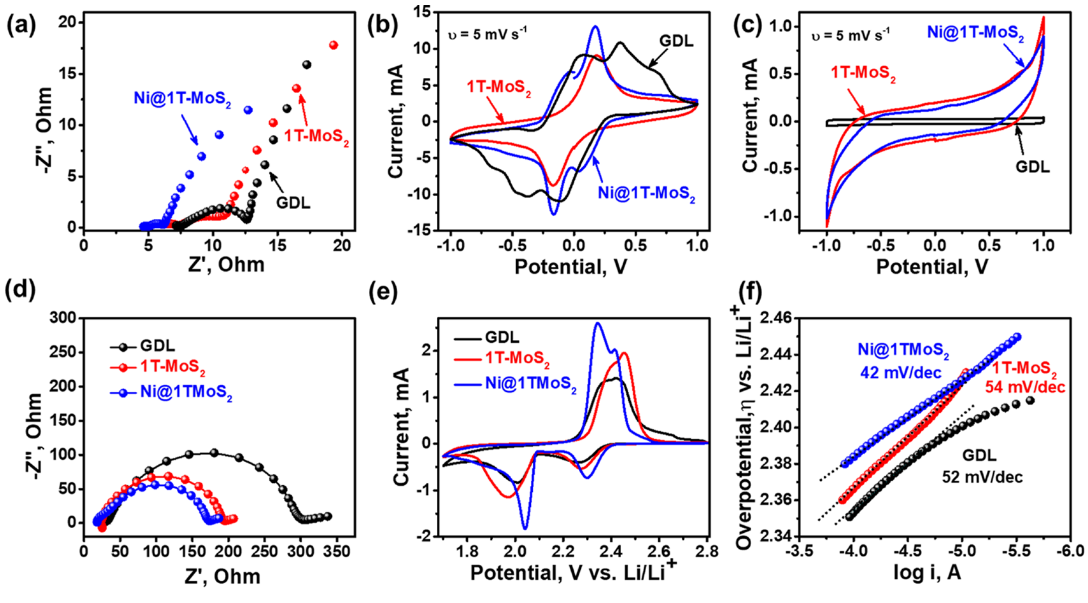

Figure 4. Evaluation of catalytic properties: (a) Nyquist plots, (b) CV with Li$_2$S$_6$, and (c) CV without Li$_2$S$_6$ of symmetric cells employing GDL, 1TMoS$_2$, and Ni@1TMoS$_2$ as working electrodes. (d) Nyquist plot and (e) CV curves recorded in the range of 1.7 to 2.8 V at a scan rate of 0.05 mV s^{-1}. (f) Tafel plots for the initial reduction reaction of GDL, 1TMoS$_2$, and Ni@1TMoS$_2$ cathodes against metallic lithium as the anode.

Ni@1TMoS$_2$ with Li$_2$S$_6$ catholytes displayed two distinct cathodic peaks at 0.038 and −0.16 V along with two anodic peaks at −0.038 and 0.16 V, indicating a highly reversible nature of the LiPS redox reaction on these electrodes. Since the Li$_2$S$_6$ is the only electrochemically active species in the symmetric cells, the four redox peaks of Ni@1TMoS$_2$ can be ascribed to (a) reduction of Li$_2$S$_6$ to discharge end products (Li$_2$S/Li$_2$S$_2$), (b) oxidation of discharge end products to Li$_2$S$_6$, (c) subsequent conversion of Li$_2$S$_6$ to sulfur, and (d) reduction of sulfur to Li$_2$S$_6$. Meanwhile, 1TMoS$_2$ exhibited anodic and cathodic peaks at 0.18 and −0.17 V, respectively, and the GDL electrode displayed a broad voltammogram with several redox peaks. A positive shift in the cathodic peaks and a negative shift in the anodic peaks with a higher current can be clearly observed for the Ni@1TMoS$_2$ electrodes when compared with 1TMoS$_2$. It is noteworthy to mention that the existence of distinct peaks with narrow separation and the peak shifts observed confirm excellent electrochemical reversibility and facile conversion of polysulfides on Ni@1TMoS$_2$. Hence, employing an electrocatalyst, MoS$_2$ doped with 3d transition metal atoms, is hypothesized to show the following effects on the Li-S system: (i) inhibiting the PS shuttle phenomenon by increasing the adsorption capability through interaction and (ii) exhibiting strong catalytic activity toward liquid LiPS redox reactions.

Further, to evaluate the electrocatalytic effect of Ni@1TMoS$_2$ on the entire sulfur lithiation/delithiation process, we have performed EIS and cyclic voltammetric studies on these electrodes. For this purpose, we have fabricated the standard 2032-coin cells and compared them with other control electrodes. The cells were assembled with the corresponding materials as working electrodes and lithium foil as a counter cum reference electrode, sandwiched with a Celgard membrane as the separator between them. For electrochemical studies, the active material was in the form of solid sulfur (1.5 mg cm^{-2}), and an appropriate amount of blank electrolyte was used. Figure 4d represents the Nyquist plots of the coin cells recorded in the frequency range of 1 MHz to 100 mHz, and the equivalent circuit is shown in Figure S6. In the high-frequency region, the intercept on the real axis is generally attributed to the ohmic resistance, while the semicircle represents the Li$^+$ charge transfer resistance at the electrode−electrolyte interface. As evidenced by the Nyquist plot, the semicircle for the Ni@1TMoS$_2$ cell is only half of the GDL cell and comparatively smaller than 1TMoS$_2$. From the fitted data (Table S3), it can be noted that while the electrolyte resistances are almost similar for all the cells (~23 Ω), the value of R2 for GDL is twice that of the Ni@1TMoS$_2$, indicating that the interface with electrocatalyst can exhibit low polarization and overpotential for entire LiPS redox reactions in the Li-S system.

Figure 4e shows the recorded cyclic voltammogram on Ni@1TMoS$_2$, 1TMoS$_2$, and bare GDL electrodes in the voltage range of 1.7 to 2.8 V vs Li/Li$^+$ at a scan rate of 0.05 mV s^{-1}. During the cathodic scan, two characteristic reduction peaks corresponding to the conversion of long-chain LiPS to medium-chain LiPS and further conversion to Li$_2$S/Li$_2$S$_2$, respectively, were observed for all the cells. Interestingly, at the long-chain LiPS reaction, an evident anodic shift in the reduction potential was observed for Ni@1TMoS$_2$ (2.34 V vs Li/Li$^+$) compared to 1TMoS$_2$ (2.27 V vs Li/Li$^+$) and GDL (2.26 V vs Li/Li$^+$). A similar observation can be made in the case of an intermediate LiPS reaction where the cells demonstrated reduction potentials of 2.04, 1.96, and 2.00 V vs Li/Li$^+$ for Ni@1TMoS$_2$, 1TMoS$_2$, and GDL, respectively. These results indicate a facile conversion of LiPS from both solid to soluble (S$_8$ to Li$_2$S$_x$, $x = 6, 8$) and soluble to insoluble states (Li$_2$S/Li$_2$S$_2$) on the Ni@1TMoS$_2$ surface. On the anodic scan, a broad oxidation peak was seen for GDL (at 2.34 V vs Li/Li$^+$) and 1TMoS$_2$ (at 2.34 V vs Li/Li$^+$), which can be attributed to the conversion of short-chain LiPS to long-chain LiPS. On the other hand, the anodic scan of Ni@1TMoS$_2$ revealed two distinct oxidation peaks, which corresponds to the effective conversion of lower-order LiPS (Li$_2$S) to medium-order LiPS (at 2.31 V vs Li/Li$^+$) and then to elemental sulfur (at 2.34 V vs Li/Li$^+$), evidencing better reversibility of the redox reactions. More importantly, a clear cathodic shift in the oxidation peak was observed for the Ni@1TMoS$_2$ compared to other electrodes. The potential difference between the first cathodic and anodic peak ($\Delta E_p = E_{pa} - E_{pc}$) was found to be 41, 44, and 30 mV for GDL, 1TMoS$_2$, and Ni@1TMoS$_2$ electrodes, respectively (Table S4). The shift in oxidation/reduction potential and the decreasing ΔE_p value in the case of Ni@1TMoS$_2$ indicates a decrease in polarization voltage between the redox reactions, while an increase in its peak currents (i_{pc}, i_{pa}) demonstrates an enhanced catalytic activity toward LiPS conversion reactions, which can be expected to improve the lifetime of Li-S performance.

To discern the kinetics of Li-S redox reactions with a quantifiable parameter, Tafel slopes and exchange current densities were derived from the linear polarization curve, as shown in Figure 4f. The exchange current densities (i_o), which reveal the charge transfer rate occurring at the catalyst surface, were obtained by extrapolating the current (x)-axis in the Tafel plot. The onset potential for the reduction of S$_8$ to long-chain LiPS was found to decrease in the case of Ni@1TMoS$_2$ compared to other materials (zoomed part of cyclic voltammogram, Figure S7). The Tafel slope and i_o values for this reduction process (at ~2.4 V) were found to be 52, 54, and 42 mV/dec and 0.142, 0.23, and 0.83 mA cm^{-2} for GDL, 1TMoS$_2$, and Ni@1TMoS$_2$, respectively. The lower Tafel slope and high i_o for Ni@1TMoS$_2$ show that the reduction of sulfur to long-chain LiPS is facilitated on its surface. Further, a similar trend was observed during the next reduction process at ~2.0 V, where the Tafel slope and i_o values were noted to be 103, 72, and 50 mV/dec and 0.304, 0.279, and 0.387 mA cm^{-2} for GDL, 1TMoS$_2$, and Ni@1TMoS$_2$, respectively. Such an evident decrease in the Tafel slope and the increased i_o for the Ni@1TMoS$_2$ electrode demonstrate a facile conversion of LiPS from soluble (liquid PS) to insoluble (solid Li$_2$S/Li$_2$S$_2$) states.[69] This can be certainly due to the fact that the LiPS undergo surface adsorption onto Ni@1TMoS$_2$, where the rate of their conversion is enhanced as evidenced by fast electron transfer kinetics. Furthermore, during the oxidation process, the derived Tafel slope (Figure S8) and i_o values were found to be 82, 182, and 52 mV/dec and 2.12, 0.789, and 2.709 mA cm^{-2} for GDL, 1TMoS$_2$, and Ni@1TMoS$_2$, respectively, which indicates that Ni@1TMoS$_2$ promoted the conversion of Li$_2$S/Li$_2$S$_2$ into long-chain LiPS without allowing them to aggregate.[20,21]

To understand the mobility of Li-ions due to the incorporation of the electrocatalyst, we made an effort to quantify the Li-ion diffusion during the sulfur redox process using the Randles−Sevcik equation $i_p = (2.65 \times 10^5) n^{1.5} S D_{Li^+}^{0.5} \Delta C_{Li} \nu^{0.5}$, where, i_p is the peak current, n is the number of electrons, S is the geometric area of the electrode, $D_{Li^+}^{0.5}$ is the

Li-ion diffusion coefficient, ΔC_{Li} is the Li-ion concentration change in the electrochemical reaction, and ν is the scan rate.[70] As shown in Figures S9,S10, the cathodic and anodic peak currents (i_p) demonstrated an excellent linear relationship with the square root of scan rates ($\nu^{0.5}$), indicating a diffusion-controlled process.[71] The obtained D_{Li^+} values for the Ni@1TMoS$_2$ electrode were found to be $D_{Li^+}^{c_1} = 2.45 \times 10^{-7}$, $D_{Li^+}^{c_2} = 2.96 \times 10^{-7}$, and $D_{Li^+}^{a_1} = 4.36 \times 10^{-7}$, which were higher than the MoS$_2$ and GDL electrodes (Table S5). Among all electrodes, GDL displayed the lowest Li$^+$ diffusion indicating a very limited surface activity toward LiPS redox. On the other hand, MoS$_2$ also demonstrated an inferior Li$^+$ diffusion coefficient, which can be certainly due to its higher charge resistance (Table S3) compared to Ni@1TMoS$_2$. In contrast, the D_{Li^+} for the Ni@1TMoS$_2$ was found to be at least one order higher than any of the contemporary electrodes (Table S6). This can be certainly due to the fact that atomically doping Ni into MoS$_2$ increases the electronic conductivity of the material, thereby enhancing the charge transfer process, which reflects as higher Li$^+$ diffusion in the cell. The electrocatalytic mechanism of Ni@1TMoS$_2$ toward LiPS redox reaction is as follows: During the sulfur redox reaction, the LiPS species adsorb onto the Ni atoms in the Ni@1TMoS$_2$ where they undergo oxidation/reduction, while the Ni surface oxidation state changes. Such interaction between the Ni and LiPS species leads to the Ni−sulfide bond formation during discharge, which is evidenced by the in situ Raman spectroscopy measurements (Figure 3). Subsequently, during charging, the oxidized Ni surface undergoes reduction, while polysulfides get oxidized. Hence, polysulfides will go through an electrochemical reversible adsorption/desorption process on the Ni surface, which was reported in our previous studies.[20] In contrast, adsorption of LiPS species adsorbed onto the Mo and S edges is purely based on charge transfer rather than direct bond formation. Catalytically active edge sites present in the MoS$_2$ including Mo and S have unsaturated dangling bonds that tend to interact with polysulfides more strongly and thus allow the LiPS reduction/oxidation on their surface. In short, the obtained kinetic parameters indicate the superior electrocatalytic activity of Ni@1TMoS$_2$ on LiPS redox reactions, which is expected to provide an excellent charge/discharge performance along with round-trip efficiency.

3.4. Electrochemical Performance. To monitor the electrochemical performance of Ni@1TMoS$_2$ nanosheets in the Li-S batteries, galvanostatic charge−discharge studies were carried out on Ni@1TMoS$_2$ in comparison with control samples of 1TMoS$_2$ and bare GDL in the potential region between 2.8 and 1.7 V, at a constant current rate of 0.1C rate. Figure 5a clearly depicts two well-defined discharge plateaus for Ni@1TMoS$_2$ (2.26 and 2.09 V vs Li/Li$^+$), 1TMoS$_2$ (2.20 and 2.04 V vs Li/Li$^+$), and GDL cathodes (2.19 and 2.01 V vs Li/Li$^+$) corresponding to reduction of S$_8$ to medium-chain LiPS (Li$_2$S$_n$, $n \geq 4$) and short-chain LiPS (Li$_2$S$_n$, $n = 1{-}3$), respectively. Herein, the Ni@1TMoS$_2$ electrode exhibits reduced polarization, which is in good agreement with CV results, with a value of 0.19 V compared to 0.26 and 0.29 V for 1TMoS$_2$ and bare GDL, indicating enhanced reaction kinetics for LiPS conversion reactions in the case of Ni@1TMoS$_2$. More importantly, during charging, the plateau at the lower potential in the case of Ni@1TMoS$_2$ indicates the conversion of short-chain LiPS to electrochemically active long-chain LiPS, which hinders the loss of active material in the form of electrochemically inactive Li$_2$S. The Ni@1TMoS$_2$ electrodes exhibited a specific capacity of 1107 mA h g^{-1} at a current rate of 0.2C over 100 cycles (Figure 5b). The enhanced cycle life was attributed to the electrocatalytic nature of Ni@1TMoS$_2$ in the conversion of short-chain LiPS to S$_8$ and vice versa. On the other hand, with a constant decay in capacity, 1TMoS$_2$ and GDL electrodes delivered a capacity of 673 and 633 mA h g^{-1} at the end of the 100th cycle.

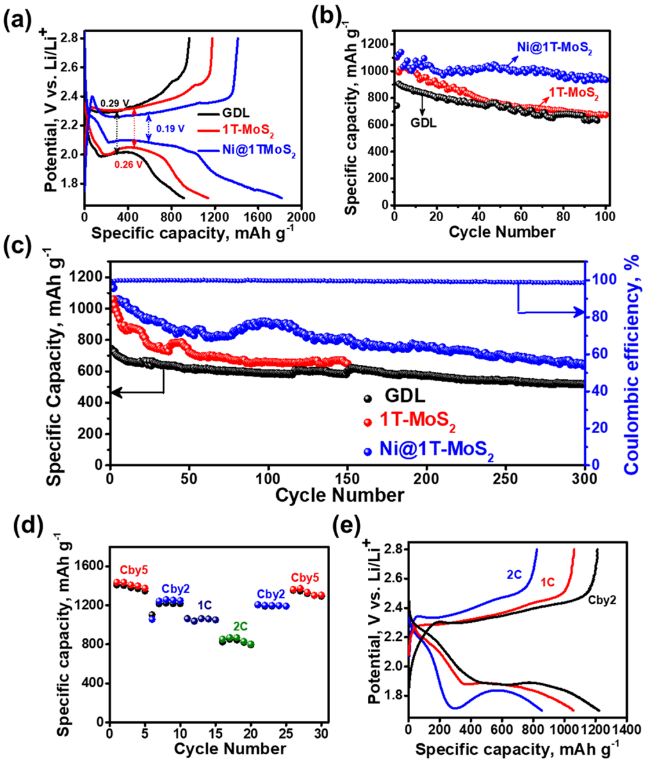

Figure 5. Electrochemical characterizations: (a) voltage vs specific capacity profile at a current rate of 0.1C; galvanostatic charge discharge behavior and coulombic efficiency at a current rate of (b) 0.2C and (c) 1C of GDL, 1TMoS$_2$, and Ni@1TMoS$_2$ electrodes vs Li/Li$^+$. (d) Rate capability and (e) voltage vs specific capacity profiles at high current rates for the Ni@1TMoS$_2$ electrode.

The Ni@1TMoS$_2$ electrode was further subjected to long cycling performance at a 1C rate and exhibited a stable performance with a minimal capacity loss of 0.19% per cycle (Figure 5c). At a 1C rate, Ni@1TMoS$_2$ electrodes delivered a capacity of 918 mA h g^{-1} for 100 cycles, and at the end of the 300th cycle, the cell delivered a capacity of 653 mA h g^{-1} with an excellent Coulombic efficiency of >99.5% throughout cycling. Meanwhile, 1TMoS$_2$ electrodes showed a severe capacity fade delivering a capacity of 655 mA h g^{-1} at the end of the 150th cycle with a capacity fade of 0.28% per cycle. Similarly, GDL also showed a drastic capacity fade while delivering a capacity of only 600 and 517 mA h g^{-1} at the end of the 150th and 300th cycles, respectively. A slight fluctuation in cell capacity during the midway of cycling was observed, which can originate from the change in carbon surface area and variations in electrode resistance during cycling. These effects induce changes in the reactivity of polysulfides with lithium ion, which leads to a variation in the sulfur utilization during each cycle. In addition, the surface area changes lead to irregular plating of discharge (Li$_2$S/Li$_2$S$_2$)/charge (S$_8$) products in each cycle, thus resulting in variations in the cathode surface resistance and fluctuation in capacity values. Furthermore, the electrodes were subjected to high-rate capability studies, and the data is presented in Figure 5d. Figure 5e shows the charge-discharge profile recorded during the rate capability studies of Ni@1TMoS$_2$ by varying the current densities from 0.2C to 2C. As can be clearly seen from the plot, the cell showed discharge capacities of 1400, 1258, 1062, and 869 mA h g^{-1} at 0.2, 0.5, 1, and 2C, respectively. Finally, when the current density of 0.2C was applied again to the cell, it still displayed a reversible discharge capacity of 1363 mA h g^{-1}. The well-defined plateaus in charge/discharge even with high C rates indicate accelerated reaction kinetics by the Ni@1TMoS$_2$ electrocatalyst on LiPS redox reactions. Therefore, the employment of the electrocatalytically active Ni@1TMoS$_2$ as electrode materials to simultaneously adsorb all intermediate LiPS and to enhance their conversions was validated by the stable battery performance.

4. CONCLUSIONS

In summary, herein, we demonstrate that the LiPS adsorption capability of electrocatalytic TMD-based sulfur hosts can be tuned by a transition metal doping strategy. UV−vis and NMR spectroscopy revealed that Ni doping on MoS$_2$ atomic sites has shown a remarkable absorption capability toward all the intermediate liquid lithium polysulfides (Li$_2$S$_x$; x = 4−8). Further, in situ Raman spectroscopy has revealed that both Ni and Mo act as binding sites for LiPS during the discharge process. Such a phenomenon was ascribed to increased active sites on the material due to doping of Ni onto basal planes of MoS$_2$ and its modified electronic structure, which synergistically contributes to LiPS adsorption. The Ni@1TMoS$_2$ was also found to act as an excellent electrocatalyst, enhancing the overall redox kinetics of sulfur redox reaction as evidenced by typical electrochemical characterizations. More importantly, Ni@1TMoS$_2$ displayed an excellent catalytic activity on the liquid to solid LiPS conversion reaction as evidenced by the decreased Tafel slope and increased exchange current density. Subsequently, the Ni@1TMoS$_2$ electrode achieved very high specific capacities of 1107 mA h g^{-1} at a current rate of 0.2 C, with a high Coulombic efficiency of ∼99%. This cathode also displayed a high rate of performance and excellent cycling stability at a current rate of 1C for over 300 cycles. The current work paves a way for the development of a new cost-efficient cathode surface with strong capability toward adsorbing and converting intermediate LiPS to end products, for high-capacity and long-life Li-S batteries.

■ ASSOCIATED CONTENT

Supporting Information

The Supporting Information is available free of charge at https://pubs.acs.org/doi/10.1021/acsami.0c04281.

> TEM images, EDAX mapping, XRD, and Raman and XPS spectra of the 1TMoS$_2$ and Ni@1TMoS$_2$; Tafel plots, cyclic voltammetry, linear relationship between cathodic peak current recorded on GDL, 1TMoS$_2$, and Ni@1TMoS$_2$ electrodes; tables representing LiPS adsorption capabilities, Raman peak assignments, comparison of LiPS charge transfer variations and kinetic parameters on different electrodes; comparison of Li$^+$ diffusion coefficients on different electrodes (PDF)

■ AUTHOR INFORMATION

Corresponding Authors

Naresh Kumar Thangavel − *Department of Mechanical Engineering, Wayne State University, Detroit, Michigan 48202, United States*; orcid.org/0000-0002-6604-0211; Email: ge4108@wayne.edu

Leela Mohana Reddy Arava − *Department of Mechanical Engineering, Wayne State University, Detroit, Michigan 48202, United States*; orcid.org/0000-0001-6685-6061; Email: leela.arava@wayne.edu

Authors

Kiran Mahankali − *Department of Mechanical Engineering, Wayne State University, Detroit, Michigan 48202, United States*; orcid.org/0000-0003-3540-5350

Daryna Gopchenko − *Department of Mechanical Engineering, Wayne State University, Detroit, Michigan 48202, United States*

Complete contact information is available at: https://pubs.acs.org/10.1021/acsami.0c04281

Notes

The authors declare no competing financial interest.

■ ACKNOWLEDGMENTS

This article was supported in part by the National Science Foundation under grant no. 1751472 and ACSPetroleum Research Fund (ACSPRF: 57647-DNI10). The authors thank the Lumigen Instrument Centre at Wayne State University for the use of PXRD (NSF:MRI1427926) and JEOL 2010 TEM (NSF:MRI - 0216084) and 400MHz NMR (NSF:MRI - 0840413) facilities.

■ REFERENCES

(1) Manthiram, A.; Fu, Y.; Chung, S. H.; Zu, C.; Su, Y. S. Rechargeable lithium-sulfur batteries. *Chem. Rev.* **2014**, *114*, 11751−11787.

(2) Bruce, P. G.; Freunberger, S. A.; Hardwick, L. J.; Tarascon, J. M. Li-O$_2$ and Li-S batteries with high energy storage. *Nat. Mater.* **2011**, *11*, 19−29.

(3) Miroshnikov, M.; Mahankali, K.; Thangavel, N. K.; Satapathy, S.; Arava, L. M. R.; Ajayan, P. M.; John, G. Bioderived Molecular Electrodes for Next Generation Energy Storage Materials. *ChemSusChem* **2020**, *13*, 2186−2204.

(4) Bresser, D.; Passerini, S.; Scrosati, B. Recent progress and remaining challenges in sulfur-based lithium secondary batteries—a review. *Chem. Commun.* **2013**, *49*, 10545−10562.

(5) Song, M. K.; Cairns, E. J.; Zhang, Y. Lithium/sulfur batteries with high specific energy: old challenges and new opportunities. *Nanoscale* **2013**, *5*, 2186−2204.

(6) Pang, Q.; Liang, X.; Kwok, C. Y.; Nazar, L. F. Advances in lithium−sulfur batteries based on multifunctional cathodes and electrolytes. *Nat. Energy* **2016**, *1*, 16132.

(7) Zhang, B.; Qin, X.; Li, G. R.; Gao, X. P. Enhancement of long stability of sulfur cathode by encapsulating sulfur into micropores of carbon spheres. *Energy Environ. Sci.* **2010**, *3*, 1531−1537.

(8) Schuster, J.; He, G.; Mandlmeier, B.; Yim, T.; Lee, K. T.; Bein, T.; Nazar, L. F. Spherical ordered mesoporous carbon nanoparticles with high porosity for lithium−sulfur batteries. *Angew. Chem., Int. Ed.* **2012**, *51*, 3591−3595.

(9) Jayaprakash, N.; Shen, J.; Moganty, S. S.; Corona, A.; Archer, L. A. Porous hollow carbon@ sulfur composites for high-power lithium−sulfur batteries. *Angew. Chem. Int. Ed.* **2011**, *50*, 5904−5908.

(10) Guo, J.; Xu, Y.; Wang, C. Sulfur-impregnated disordered carbon nanotubes cathode for lithium−sulfur batteries. *Nano Lett.* **2011**, *11*, 4288−4294.

(11) Zheng, G.; Yang, Y.; Cha, J. J.; Hong, S. S.; Cui, Y. Hollow carbon nanofiber-encapsulated sulfur cathodes for high specific capacity rechargeable lithium batteries. *Nano Lett.* **2011**, *11*, 4462−4467.

(12) Ji, L.; Rao, M.; Zheng, H.; Zhang, L.; Li, Y.; Duan, W.; Guo, J.; Cairns, E. J.; Zhang, Y. Graphene oxide as a sulfur immobilizer in high performance lithium/sulfur cells. *J. Am. Chem. Soc.* **2011**, *133*, 18522−18525.

(13) Ji, X.; Lee, K. T.; Nazar, L. F. A highly ordered nanostructured carbon−sulphur cathode for lithium−sulphur batteries. *Nat. Mater.* **2009**, *8*, 500−506.

(14) Peng, H. J.; Zhang, G.; Chen, X.; Zhang, Z. W.; Xu, W. T.; Huang, J. Q.; Zhang, Q. Enhanced Electrochemical Kinetics on Conductive Polar Mediators for Lithium-Sulfur Batteries. *Angew. Chem. Int. Ed.* **2016**, *55*, 12990−12995.

(15) Song, J.; Gordin, M. L.; Xu, T.; Chen, S.; Yu, Z.; Sohn, H.; Lu, J.; Ren, Y.; Duan, Y.; Wang, D. Strong lithium polysulfide chemisorption on electroactive sites of nitrogen-doped carbon composites for high-performance lithium-sulfur battery cathodes. *Angew. Chem. Int. Ed.* **2015**, *54*, 4325−4329.

(16) Pang, Q.; Liang, X.; Kwok, C. Y.; Nazar, L. F. Review-The Importance of Chemical Interactions between Sulfur Host Materials and Lithium Polysulfides for Advanced Lithium-Sulfur Batteries. *J. Electrochem. Soc.* **2015**, *162*, A2567−A2576.

(17) Pang, Q.; Kundu, D.; Cuisinier, M.; Nazar, L. F. Surface-enhanced redox chemistry of polysulphides on a metallic and polar host for lithium-sulphur batteries. *Nat. Commun* **2014**, *5*, 4759−4767.

(18) Fan, X.; Sun, W.; Meng, F.; Xing, A.; Liu, J. Advanced chemical strategies for lithium−sulfur batteries: A review. *Green. Energy. Environ.* **2018**, *3*, 2−19.

(19) Babu, G.; Ababtain, K.; Ng, K. Y. S.; Arava, L. M. R. Electrocatalysis of lithium polysulfides: current collectors as electrodes in Li/S battery configuration. *Sci. Rep.* **2015**, *5*, 8763−8770.

(20) Al Salem, H.; Babu, G.; Rao, C. V.; Arava, L. M. R. Electrocatalytic polysulfide traps for controlling redox shuttle process of Li−S batteries. *J. Am. Chem. Soc.* **2015**, *137*, 11542−11545.

(21) Babu, G.; Masurkar, N.; Al Salem, H.; Arava, L. M. R. Transition metal dichalcogenide atomic layers for lithium polysulfides electrocatalysis. *J. Am. Chem. Soc.* **2016**, *139*, 171−178.

(22) Li, W.; Zhang, Q.; Zheng, G.; Seh, Z. W.; Yao, H.; Cui, Y. Understanding the role of different conductive polymers in improving the nanostructured sulfur cathode performance. *Nano Lett.* **2013**, *13*, 5534−5540.

(23) Demir-Cakan, R.; Morcrette, M.; Nouar, F.; Davoisne, C.; Devic, T.; Gonbeau, D.; Dominko, R.; Serre, C.; Férey, G.; Tarascon, J. M. Cathode composites for Li−S batteries via the use of oxygenated porous architectures. *J. Am. Chem. Soc.* **2011**, *133*, 16154−16160.

(24) Zhang, Z.; Lai, Y.; Zhang, Z.; Zhang, K.; Li, J. Al_2O_3-coated porous separator for enhanced electrochemical performance of lithium sulfur batteries. *Electrochim. Acta* **2014**, *129*, 55−61.

(25) Seh, Z. W.; Li, W.; Cha, J. J.; Zheng, G.; Yang, Y.; McDowell, M. T.; Hsu, P. C.; Cui, Y. Sulphur−TiO_2 yolk−shell nanoarchitecture with internal void space for long-cycle lithium−sulphur batteries. *Nat. Commun.* **2013**, *4*, 1331−1337.

(26) Zhou, G.; Tian, H.; Jin, Y.; Tao, X.; Liu, B.; Zhang, R.; Seh, Z. W.; Zhuo, D.; Liu, Y.; Sun, J.; Zhao, J.; Zu, C.; Wu, D. S.; Zhang, Q.; Cui, Y. Catalytic oxidation of Li_2S on the surface of metal sulfides for Li−S batteries. *Proc. Natl. Acad. Sci.* **2017**, *114*, 840−845.

(27) Lin, H.; Yang, L.; Jiang, X.; Li, G.; Zhang, T.; Yao, Q.; Zheng, G. W.; Lee, J. Y. Electrocatalysis of polysulfide conversion by sulfur-deficient MoS_2 nanoflakes for lithium−sulfur batteries. *Energy Environ. Sci.* **2017**, *10*, 1476−1486.

(28) Liang, X.; Liu, Y.; Wen, Z.; Huang, L.; Wang, X.; Zhang, H. A nano-structured and highly ordered polypyrrole-sulfur cathode for lithium−sulfur batteries. *J. Power Sources* **2011**, *196*, 6951−6955.

(29) Yang, Y.; Yu, G.; Cha, J. J.; Wu, H.; Vosgueritchian, M.; Yao, Y.; Bao, Z.; Cui, Y. Improving the performance of lithium−sulfur batteries by conductive polymer coating. *ACS Nano* **2011**, *5*, 9187−9193.

(30) Xiao, L.; Cao, Y.; Xiao, J.; Schwenzer, B.; Engelhard, M. H.; Saraf, L. V.; Nie, Z.; Exarhos, G. J.; Liu, J. A soft approach to encapsulate sulfur: polyaniline nanotubes for lithium-sulfur batteries with long cycle life. *Adv. Mater.* **2012**, *24*, 1176−1181.

(31) Wang, X.; Gao, T.; Fan, X.; Han, F.; Wu, Y.; Zhang, Z.; Li, J.; Wang, C. Tailoring Surface Acidity of Metal Oxide for Better Polysulfide Entrapment in Li-S Batteries. *Adv. Funct. Mater.* **2016**, *26*, 7164−7169.

(32) Tao, X.; Wang, J.; Liu, C.; Wang, H.; Yao, H.; Zheng, G.; Seh, Z. W.; Cai, Q.; Li, W.; Zhou, G.; Zu, C.; Cui, Y. Balancing surface adsorption and diffusion of lithium-polysulfides on nonconductive oxides for lithium−sulfur battery design. *Nat. Commun.* **2016**, *7*, 11203−11212.

(33) Liu, X.; Huang, J. Q.; Zhang, Q.; Mai, L. Nanostructured metal oxides and sulfides for lithium−sulfur batteries. *Adv. Mater.* **2017**, *29*, 1601759.

(34) Yuan, Z.; Peng, H. J.; Hou, T. Z.; Huang, J. Q.; Chen, C. M.; Wang, D. W.; Cheng, X. B.; Wei, F.; Zhang, Q. Powering lithium−sulfur battery performance by propelling polysulfide redox at sulfiphilic hosts. *Nano Lett.* **2016**, *16*, 519−527.

(35) Peng, H. J.; Zhang, Z. W.; Huang, J. Q.; Zhang, G.; Xie, J.; Xu, W. T.; Shi, J. L.; Chen, X.; Cheng, X. B.; Zhang, Q. A Cooperative Interface for Highly Efficient Lithium−Sulfur Batteries. *Adv. Mater.* **2016**, *28*, 9551−9558.

(36) Zhang, Q.; Wang, Y.; Seh, Z. W.; Fu, Z.; Zhang, R.; Cui, Y. Understanding the anchoring effect of two-dimensional layered materials for lithium−sulfur batteries. *Nano Lett.* **2015**, *15*, 3780−3786.

(37) Kamphaus, E. P.; Balbuena, P. B. Long-chain polysulfide retention at the cathode of Li−S batteries. *J. Phys. Chem. C* **2016**, *120*, 4296−4305.

(38) Ghosh, A.; Garapati, M. S.; Vijaya Kumar Saroja, A. P.; Sundara, R. Polar Bilayer Cathode for Advanced Lithium-Sulfur Battery: Synergy Between Polysulfide Conversion and Confinement. *J. Phys. Chem. C* **2019**, *123*, 10777−10787.

(39) Huang, Y.; Sun, Y.; Zheng, X.; Aoki, T.; Pattengale, B.; Huang, J.; He, X.; Bian, W.; Younan, S.; Williams, N.; Hu, J.; Ge, J.; Pu, N.; Yan, X.; Pan, X.; Zhang, L.; Wei, Y.; Gu, J. Atomically engineering activation sites onto metallic 1T-MoS_2 catalysts for enhanced electrochemical hydrogen evolution. *Nat. Commun.* **2019**, *10*, 982.

(40) Mahankali, K.; Thangavel, N. K.; Ding, Y.; Putatunda, S. K.; Arava, L. M. R. Interfacial behavior of water-in-salt electrolytes at porous electrodes and its effect on supercapacitor performance. *Electrochim. Acta* **2019**, *326*, 134989−134997.

(41) Mahankali, K.; Thangavel, N. K.; Reddy Arava, L. M. In Situ Electrochemical Mapping of Lithium−Sulfur Battery Interfaces Using AFM−SECM. *Nano Lett.* **2019**, *19*, 5229−5236.

(42) Miroshnikov, M.; Kato, K.; Babu, G.; Thangavel, N. K.; Mahankali, K.; Hohenstein, E.; Wang, H.; Satapathy, S.; Divya, K. P.; Asare, H.; Ajayan, P. M.; Arava, L. M. R.; John, G. Made From Henna! A Fast-Charging, High-Capacity, and Recyclable Tetrakislawsone Cathode Material for Lithium ion Batteries. *ACS Sustainable Chem. Eng.* **2019**, *7*, 13836−13844.

(43) Geng, X.; Sun, W.; Wu, W.; Chen, B.; Al-Hilo, A.; Benamara, M.; Zhu, H.; Watanabe, F.; Cui, J.; Chen, T.-P. Pure and stable metallic phase molybdenum disulfide nanosheets for hydrogen evolution reaction. *Nat. Commun.* **2016**, *7*, 10672.

(44) Zhang, X. J.; Wang, S. W.; Wang, G. S.; Li, Z.; Guo, A. P.; Zhu, J. Q.; Liu, D. P.; Yin, P. G. Facile synthesis of NiS_2@MoS_2 core-shell nanospheres for effective enhancement in microwave absorption. *RSC Adv.* **2017**, *7*, 22454−22460.

(45) Liu, Q.; Li, X.; He, Q.; Khalil, A.; Liu, D.; Xiang, T.; Wu, X.; Song, L. Gram-scale aqueous synthesis of stable few-layered 1T-MoS_2: applications for visible-light-driven photocatalytic hydrogen evolution. *Small* **2015**, *11*, 5556−5564.

(46) Wang, D.; Zhang, X.; Shen, Y.; Wu, Z. Ni-doped MoS_2 nanoparticles as highly active hydrogen evolution electrocatalysts. *RSC Adv.* **2016**, *6*, 16656−16661.

(47) Houssenbay, S.; Kasztelan, S.; Toulhoat, H.; Bonnelle, J. P.; Grimblot, J. Nature of the different nickel species in sulfided bulk and alumina-supported nickel-molybdenum hydrotreating catalysts. *J. Phys. Chem.* **1989**, *93*, 7176−7180.

(48) Hu, L.; Dai, C.; Lim, J. M.; Chen, Y.; Lian, X.; Wang, M.; Li, Y.; Xiao, P.; Henkelman, G.; Xu, M. A highly efficient double-hierarchical sulfur host for advanced lithium−sulfur batteries. *Chem. Sci.* **2018**, *9*, 666−675.

(49) Barchasz, C.; Molton, F.; Duboc, C.; Leprêtre, J. C.; Patoux, S.; Alloin, F. Lithium/sulfur cell discharge mechanism: an original approach for intermediate species identification. *Anal. Chem.* **2012**, *84*, 3973−3980.

(50) Wu, D. S.; Shi, F.; Zhou, G.; Zu, C.; Liu, C.; Liu, K.; Liu, Y.; Wang, J.; Peng, Y.; Cui, Y. Quantitative investigation of polysulfide adsorption capability of candidate materials for Li-S batteries. *Energy Storage Mater.* **2018**, *13*, 241−246.

(51) Patel, M. U. M.; Demir-Cakan, R.; Morcrette, M.; Tarascon, J. M.; Gaberscek, M.; Dominko, R. Li-S Battery Analyzed by UV/Vis in Operando Mode. *ChemSusChem* **2013**, *6*, 1177−1181.

(52) Ni, X.; Qian, T.; Liu, X.; Xu, N.; Liu, J.; Yan, C. High Lithium Ion Conductivity LiF/GO Solid Electrolyte Interphase Inhibiting the Shuttle of Lithium Polysulfides in Long-Life Li−S Batteries. *Adv. Funct. Mater.* **2018**, *28*, 1706513.

(53) Hou, T. Z.; Xu, W. T.; Chen, X.; Peng, H. J.; Huang, J. Q.; Zhang, Q. Lithium bond chemistry in lithium−sulfur batteries. *Angew. Chem., Int. Ed.* **2017**, *56*, 8178−8182.

(54) Babu, G.; Sawas, A.; Thangavel, N. K.; Arava, L. M. R. Two-Dimensional Material-Reinforced Separator for Li−Sulfur Battery. *J. Phys. Chem. C* **2018**, *122*, 10765−10772.

(55) Wang, H.; Zhang, Q.; Yao, H.; Liang, Z.; Lee, H. W.; Hsu, P. C.; Zheng, G.; Cui, Y. High electrochemical selectivity of edge versus terrace sites in two-dimensional layered MoS_2 materials. *Nano Lett.* **2014**, *14*, 7138−7144.

(56) Luo, R.; Luo, M.; Wang, Z.; Liu, P.; Song, S.; Wang, X.; Chen, M. The atomic origin of nickel-doping-induced catalytic enhancement in MoS_2 for electrochemical hydrogen production. *Nanoscale* **2019**, *11*, 7123−7128.

(57) Lau, T. H. M.; Lu, X.; Kulhavý, J.; Wu, S.; Lu, L.; Wu, T. S.; Kato, R.; Foord, J. S.; Soo, Y. L.; Suenaga, K.; Tsang, S. C. E. Transition metal atom doping of the basal plane of MoS_2 monolayer nanosheets for electrochemical hydrogen evolution. *Chem. Sci.* **2018**, *9*, 4769−4776.

(58) Wang, H.; Tsai, C.; Kong, D.; Chan, K.; Abild-Pedersen, F.; Nørskov, J. K.; Cui, Y. Transition-metal doped edge sites in vertically aligned MoS_2 catalysts for enhanced hydrogen evolution. *Nano Res.* **2015**, *8*, 566−575.

(59) Lauritsen, J. V.; Kibsgaard, J.; Olesen, G. H.; Moses, P. G.; Hinnemann, B.; Helveg, S.; Nørskov, J. K.; Clausen, B. S.; Topsøe, H.; Lægsgaard, E.; Besenbacher, F. Location and coordination of promoter atoms in Co- and Ni-promoted MoS_2-based hydrotreating catalysts. *J. Catal.* **2007**, *249*, 220−233.

(60) Zhang, Y.; Wang, R.; Tang, W.; Zhan, L.; Zhao, S.; Kang, Q.; Wang, Y.; Yang, S. Efficient polysulfide barrier of a graphene aerogel−carbon nanofibers−Ni network for high-energy-density lithium−sulfur batteries with ultrahigh sulfur content. *J. Mater. Chem. A* **2018**, *6*, 20926−20938.

(61) Dong, S.; Sun, X.; Wang, Z. Trapping polysulfide on two-dimensional molybdenum disulfide for Li−S batteries through phase selection with optimized binding. *Beilstein J. Nanotechnol.* **2019**, *10*, 774−780.

(62) Luo, J.; Wang, H.; Su, G.; Tang, Y.; Liu, H.; Tian, F.; Li, D. Self-supported nickel phosphosulphide nanosheets for highly efficient and stable overall water splitting. *J. Mater. Chem. A* **2017**, *5*, 14865−14872.

(63) Liu, W.; Hu, E.; Jiang, H.; Xiang, Y.; Weng, Z.; Li, M.; Fan, Q.; Yu, X.; Altman, E. I.; Wang, H. A highly active and stable hydrogen evolution catalyst based on pyrite-structured cobalt phosphosulfide. *Nat. Commun.* **2016**, *7*, 10771.

(64) Wang, Q.; Zheng, J.; Walter, E.; Pan, H.; Lv, D.; Zuo, P.; Chen, H.; Deng, Z. D.; Liaw, B. Y.; Yu, X.; Yang, X.; Zhang, J.-G.; Liu, J.; Xiao, J. Direct observation of sulfur radicals as reaction media in lithium sulfur batteries. *J. Electrochem. Soc.* **2015**, *162*, A474−A478.

(65) Vijayakumar, M.; Govind, N.; Walter, E.; Burton, S. D.; Shukla, A.; Devaraj, A.; Xiao, J.; Liu, J.; Wang, C.; Karim, A.; Thevuthasan, S. Molecular structure and stability of dissolved lithium polysulfide species. *Phys. Chem. Chem. Phys.* **2014**, *16*, 10923−10932.

(66) Gupta, A.; Bhargav, A.; Manthiram, A. Highly solvating electrolytes for lithium−sulfur batteries. *Adv. Energy Mater.* **2019**, *9*, 1803096−1803105.

(67) Han, D. H.; Kim, B. S.; Choi, S. J.; Jung, Y.; Kwak, J.; Park, S. M. Time-resolved in situ spectroelectrochemical study on reduction of sulfur in N, N′-dimethylformamide. *J. Electrochem. Soc.* **2004**, *151*, E283−E290.

(68) Wang, D.; Zhao, L.; Wang, D.; Yan, L.; Jing, C.; Zhang, H.; Guo, L. H.; Tang, N. Direct evidence for surface long-lived superoxide radicals photo-generated in TiO_2 and other metal oxide suspensions. *Phys. Chem. Chem. Phys.* **2018**, *20*, 18978−18985.

(69) Sawas, A.; Babu, G.; Thangavel, N. K.; Arava, L. M. R. Electrocatalysis driven high energy density Li-ion polysulfide battery. *Electrochim. Acta* **2019**, *307*, 253−259.

(70) Thangavel, N. K.; Gopalakrishnan, D.; Arava, L. M. R. Understanding Heterogeneous Electrocatalysis of Lithium Polysulfide Redox on Pt and WS_2 Surfaces. *J. Phys. Chem. C* **2017**, *121*, 12718−12725.

(71) Gao, X.; Zhou, D.; Chen, Y.; Wu, W.; Su, D.; Li, B.; Wang, G. Strong charge polarization effect enabled by surface oxidized titanium nitride for lithium-sulfur batteries. *Commun. Chem.* **2019**, *2*, 66.

https://dx.doi.org/10.1021/acsami.0c04281
ACS Appl. Mater. Interfaces 2020, 12, 27112−27121